

A marine controlled-source electromagnetic application using towed and seafloor-based receivers capable of mapping seafloor and embedded massive sulfides

Keiichi Ishizu¹, Takafumi Kasaya², Tada-Nori Goto³, Katsuaki Koike⁴, Weerachai Siripunvaraporn⁵, Hisanori Iwamoto⁶, Yoshifumi Kawada², and Jun-Ichiro Ishibashi⁷

ABSTRACT

Deep-sea massive sulfide deposits formed by hydrothermal fluid circulation are potential metal resources. They can exist not only as mound manifestations on the seafloor (seafloor massive sulfides) but also as embedded anomalies buried beneath the seafloor (embedded massive sulfides). The distribution of embedded massive sulfides is largely unknown, despite their expected high economic value. Recent drilling surveys have revealed a complex model suggesting embedded massive sulfides coexist beneath seafloor massive sulfides. In the coexisting case, geophysical methods are required to distinguish and map seafloor and embedded massive sulfides for accurate resource estimation. Marine controlled-source electromagnetic (CSEM) methods are useful for mapping massive sulfides because they exhibit higher electrical conductivity compared with the surrounding host rock.

However, CSEM applications capable of distinguishing and mapping the massive sulfides are lacking. We use a towed electric dipole transmitter with two types of receivers: stationary ocean-bottom electric (OBE) and short-offset towed receivers. This combination uses differences in sensitivity: the towed receiver data are sensitive to seafloor massive sulfides, and the stationary OBE receiver data are sensitive to embedded massive sulfides. Our synthetic data example demonstrates that the combined inversion of towed and OBE data can recover resistivities and positions of the massive sulfides more accurately than existing inversion methods using individual applications. We perform the combined inversion of measured CSEM data obtained from the middle Okinawa Trough. The inversion models demonstrate that a combined inversion can map the location and shape of embedded massive sulfides identified during drilling more accurately than the inversion of individual data sets.

INTRODUCTION

Deep-sea massive sulfide deposits are formed by hydrothermal fluid circulation associated with subseafloor processes and are found in hydrothermally active areas such as back-arc spreading centers, midocean ridges, and volcanic arcs (Humphris et al., 1995;

Hannington et al., 2011; Ishibashi et al., 2015; Nozaki et al., 2020). They are rich in metals such as copper, lead, zinc, gold, and silver (Hannington et al., 2010; Petersen et al., 2016; Fuchs et al., 2019). Their high metal concentrations have increased the interest in exploring and assessing massive sulfide resources in deep-sea hydrothermal areas (Kowalczyk, 2008; Hannington et al., 2011;

Manuscript received by the Editor 30 June 2023; revised manuscript received 9 December 2023; published ahead of production 19 February 2024; published online 9 April 2024.

¹Kyoto University, Department of Urban Management, Kyoto, Japan; Japan Agency for Marine-Earth Science and Technology (JAMSTEC), Research Institute for Marine Resources Utilization, Kanagawa, Japan; and University of Hyogo, Graduate School of Science, Hyogo, Japan. E-mail: ishizu.keiichi.n30@kyoto-u.jp (corresponding author).

²Japan Agency for Marine-Earth Science and Technology (JAMSTEC), Research Institute for Marine Resources Utilization, Kanagawa, Japan. E-mail: tkasa@jamstec.go.jp; kawada@jamstec.go.jp.

³Kyoto University, Department of Urban Management, Kyoto, Japan and University of Hyogo, Graduate School of Science, Hyogo, Japan. E-mail: t.n.goto@sci.u-hyogo.ac.jp.

⁴Kyoto University, Department of Urban Management, Kyoto, Japan. E-mail: koike.katsuaki.5x@kyoto-u.ac.jp.

⁵Mahidol University, Department of Physics, Bangkok, Thailand and ThEP Center, Commission on Higher Education, Bangkok, Thailand. E-mail: wsiripun@gmail.com.

⁶Nippon Marine Enterprises, Ltd., Marine Survey Department, Kanagawa, Japan. E-mail: iwamotoh@nme.co.jp.

⁷Kobe University, Ocean-Bottom Exploration Center, Hyogo, Japan. E-mail: ishishashi@port.kobe-u.ac.jp.

© 2024 Society of Exploration Geophysicists. All rights reserved.

Boschen et al., 2013; Tornos et al., 2015; Monecke et al., 2016; Murton et al., 2019).

Deep-sea massive sulfides can be divided into two types based on their location: seafloor massive sulfides that are visible and frequently composed of chimney and mound structures on the seafloor (Humphris et al., 1995; Zierenberg et al., 1998) and embedded seafloor massive sulfides that are buried below the seafloor (Zierenberg et al., 1998; Takai et al., 2011; Petersen et al., 2014). Seafloor massive sulfides are discoverable by submersible surveys and can be visually identified. If seafloor massive sulfides occur with hydrothermal activity, hydrothermal plume surveys also are effective for their detection (Kasaya et al., 2015; German et al., 2016). However, submersible and plume surveys cannot determine the vertical extent of the mineralized deposit. Thus, geophysical methods, which can investigate subseafloor structures, are required for determining their spatial extents. Moreover, because submersible surveys cannot detect massive sulfides embedded within the subseafloor, their detection and delineation rely on geophysical methods and drillings.

Embedded massive sulfides have been reported in several areas such as the Okinawa Trough (Takai et al., 2011; Totsuka et al., 2019; Nozaki et al., 2021), the Palinuro Seamount (Petersen et al., 2014), and the northern Juan de Fuca spreading center (Zierenberg et al., 1998). The drill core of Ocean Drilling Program Leg 169 on the northern Juan de Fuca spreading center discovered embedded massive sulfides containing up to 50 vol% sulfide minerals at 200–210 m below the seafloor (mbsf) (Zierenberg et al., 1998). Scientific drilling by D/V Chikyu in the Okinawa Trough found cores of embedded massive sulfides enriched in copper, lead, and zinc at 5–25 mbsf and 30–65 mbsf (Nozaki et al., 2021). Previous studies interpreted that they occurred as a replacement of the host sediments (Zierenberg et al., 1998; Petersen et al., 2014; Nozaki et al., 2021), or they were initially formed on the seafloor and later buried beneath the seafloor (Nozaki et al., 2021). These drilling results revealed vertical extents and metal contents of embedded massive sulfides and pointed out their high economic value (Zierenberg et al., 1998; Petersen et al., 2016; Nozaki et al., 2021). However, their horizontal distribution has not been determined due to sparse drilling points, causing large uncertainties in their resource assessment. Therefore, determining the distribution of embedded massive sulfides is essential for more accurate resource assessment.

Drilling surveys have revealed embedded massive sulfides coexisting beneath seafloor massive sulfides, suggesting that seafloor and embedded massive sulfides not only exist individually but also can coexist (Zierenberg et al., 1998). Their coexistence has been reported in the Okinawa Trough (Takai et al., 2011; Totsuka et al., 2019; Morozumi et al., 2020; Nozaki et al., 2021) and on the northern Juan de Fuca spreading center (Zierenberg et al., 1998). Our study area, Okinawa Trough, is the most investigated in Japan for massive sulfides (Ishibashi et al., 2015). Drilling surveys have confirmed the coexistence in the Izena (Totsuka et al., 2019; Morozumi et al., 2020; Koike et al., 2022) and Iheya hydrothermal areas (Takai et al., 2011; Ishizu et al., 2019), which are representative of the massive sulfide areas in the Okinawa Trough. This indicates that the coexistence of the massive sulfides may be common in the Okinawa Trough. Therefore, geophysical applications capable of distinguishing and mapping these types of massive sulfides are essential for exploration surveys here. However, a geophysical framework for this purpose has not been established.

This study focuses on marine electromagnetic (EM) methods because they are particularly useful for massive sulfide exploration.

Massive sulfides exhibit a lower electrical resistivity than the surrounding host rock (Von Herzen et al., 1996; Spagnoli et al., 2016; Müller et al., 2018), favoring EM applications, which are sensitive to subseafloor electrical resistivity structures. Controlled-source EM (CSEM) methods are the most popular EM methods for massive sulfide exploration (Cairns et al., 1996; Swidinsky et al., 2012; Hölz and Jegen, 2016; Haroon et al., 2018; Gehrman et al., 2020). CSEM methods use a transmitter as an artificial EM energy source and receivers that record the response from the transmitter. Various transmitter and receiver configurations have been developed for CSEM methods, depending on target massive sulfides. CSEM data can be interpreted in the frequency domain or the time domain, that is, as transients. CSEM methods using transients also are referred to as transient EM (TEM) methods.

CSEM systems using short transmitter-receiver offsets of <500 m have been applied to detect seafloor massive sulfides and/or shallow embedded massive sulfides. Imamura et al. (2018) use a CSEM system with a horizontal electric dipole (HED) transmitter mounted on a remotely operated vehicle (ROV) and ocean-bottom electric (OBE) receivers with a transmitter-receiver offset of <100 m. Haroon et al. (2018) and Gehrman et al. (2019) apply a CSEM system using a towed HED transmitter and towed receivers a few hundred meters behind the transmitter. A towed loop coil transmitter-receiver system was applied for the TEM survey (Hölz and Jegen, 2016; Haroon et al., 2018) and frequency-domain CSEM survey (Müller et al., 2018). Nakayama and Saito (2016) apply an ROV-based TEM system. However, if a coexistence model of seafloor and embedded massive sulfides is considered, all the preceding CSEM methods are less sensitive to embedded massive sulfides located below the seafloor massive sulfides because of their limited depths of investigation.

CSEM systems using large transmitter-receiver offsets of <1.5 km have been applied to detect deep resistivity structures in hydrothermal areas. Constable et al. (2018) use a CSEM method with a stationary HED transmitter deployed on the seafloor and a towed receiver on an autonomous underwater vehicle (AUV). Ishizu et al. (2022) use a CSEM method with a towed HED transmitter and stationary OBE receivers. Safipour et al. (2018) apply a towed loop transmitter based on the TEM method and stationary OBE receivers. These EM systems for deep exploration are sensitive to seafloor and embedded massive sulfides (Constable et al., 2018; Safipour et al., 2018; Ishizu et al., 2022). However, their drawbacks include the limited sensitivity toward seafloor massive sulfides because of the inability to use short transmitter-receiver separation data due to large uncertainties in transmitter-receiver positioning. That is, a marine EM application capable of effectively detecting and mapping the massive sulfides is lacking.

This study presents a CSEM configuration using an HED transmitter and two types of receivers to better map these types of massive sulfides: stationary OBE and short-offset towed receivers. This receiver combination assumes that the towed receiver data, which are sensitive to seafloor massive sulfides, can complement the OBE receiver data, which exhibit limited sensitivity toward shallow structures but are sensitive to embedded massive sulfides. An advantage of the CSEM configuration is that the system has a high operational affinity because the stationary OBE and towed receivers can simultaneously record CSEM responses from the transmitter. This combined CSEM method has previously been applied to hydrocarbon exploration (Morten et al., 2016; Attias et al., 2018). It was

where w_x is the weights for the penalty in the x -direction and ∂_y and ∂_z with w_y and w_z are defined in a similar manner. We fix α_x , α_y , and α_z and all components of w_x , w_y , and w_z to one. Here, \mathbf{d} consists of OBE receiver data (\mathbf{d}_{OBE}) and towed receiver data ($\mathbf{d}_{\text{TOWED}}$) as

$$\mathbf{d} = \begin{bmatrix} \mathbf{d}_{\text{OBE}} \\ \mathbf{d}_{\text{TOWED}} \end{bmatrix}. \quad (4)$$

The dimensions of \mathbf{d}_{OBE} and $\mathbf{d}_{\text{TOWED}}$ are N_{OBE} and N_{TOWED} , respectively, and $N = N_{\text{OBE}} + N_{\text{TOWED}}$. Elements of \mathbf{d} from 1 to N_{OBE} and $N_{\text{OBE}} + 1$ to N represent OBE receiver data and towed receiver data, respectively. The inverse of the data covariance matrix is expressed as

$$\mathbf{C}_d^{-1} = \mathbf{W}_d^T \mathbf{W}_d, \quad (5)$$

where \mathbf{W}_d is the diagonal matrix of $M \times M$ (Constable et al., 1987) written as

$$\mathbf{W}_d = \text{diag} \left\{ \frac{\gamma_{\text{OBE}}}{e_1}, \dots, \frac{\gamma_{\text{OBE}}}{e_{N_{\text{OBE}}}}, \frac{\gamma_{\text{TOWED}}}{e_{N_{\text{OBE}}+1}}, \dots, \frac{\gamma_{\text{TOWED}}}{e_N} \right\}, \quad (6)$$

where γ_{OBE} and γ_{TOWED} are the weights for the OBE and towed receiver data, respectively, and e is the standard error of \mathbf{d} . We set γ_{OBE} and γ_{TOWED} to one because our synthetic test result in the next section shows that the inversion using the weight recovers the model sufficiently. Note that more elaborate selection of γ_{OBE} and γ_{TOWED} can potentially improve the inversion result (Commer and Newman, 2009; Meqbel and Ritter, 2015). The root-mean-square (rms) misfit is defined as

$$\text{rms misfit} = \sqrt{\frac{(\mathbf{d} - \mathbf{F}[\mathbf{m}])^T \mathbf{C}_d^{-1} (\mathbf{d} - \mathbf{F}[\mathbf{m}])}{N}}. \quad (7)$$

Further details on the 3D inversion code are described in Ishizu et al. (2022).

Synthetic modeling study

A synthetic modeling study was conducted to demonstrate the performance of the CSEM configuration using towed and sea-floor-based receivers for massive sulfide exploration. The measurement settings for the synthetic study follow the field data set described in the next section.

We used a test resistivity model with $10^8 \Omega\text{m}$ air, $0.3 \Omega\text{m}$ sea layer, $1 \Omega\text{m}$ seafloor sedimentary layers, and four $0.2 \Omega\text{m}$ massive sulfides (Figure 2). The flat seafloor was at a depth of $z = 1000 \text{ m}$; the sea surface was defined as $z = 0 \text{ m}$. Three massive sulfides (D1–D3) were exposed on the seafloor: D1 and D2 with dimensions of $100 \text{ m} \times 100 \text{ m} \times 20 \text{ m}$ and D3 with dimensions of $400 \text{ m} \times 100 \text{ m} \times 20 \text{ m}$. The resistivity values and sizes of the seafloor massive sulfides (D1–D3) are based on the resistivity models reported in previous studies (Haroon et al., 2018; Gehrmann et al., 2019; Ishizu et al., 2019). The embedded massive sulfides of D4, with dimensions of $400 \text{ m} \times 400 \text{ m} \times 50 \text{ m}$, lie at a top depth of $z = 1050 \text{ m}$. The shape of D4 is based on a deeply buried mineralization estimated by geostatistical simulation of drilling data from the Izena hydrothermal area (Koike et al., 2022). Therefore, D1–D4 represent realistic models of seafloor and embedded massive sulfides. Although the synthetic model assumes a flat seafloor, we incorporated seafloor topography into the 3D inversion of the measured data because topography plays a key role for recovering accurate resistivity structures in hydrothermal areas (Haroon et al., 2018).

Six OBE receivers were placed along the line $y = 300 \text{ m}$ at a spacing of 200 m (Figure 2). The MEMSYS towing lines were along the y -direction for the five profiles ($x = 0 \text{ m}$, 150 m , 300 m , 450 m , and 600 m). The towing height was set at 20 m from the seafloor based on our field observations (Ishizu et al., 2022). Each towing line contained 25 transmitting points with a spatial spacing of 50 m . The HED transmitter was oriented along the y -direction. The OBE and towed receivers simultaneously recorded the y -components of electric fields (E_y , V/Am^2) generated by the transmitter, which were normalized by the transmitter dipole moment (Am). All data with a transmitter-receiver offset of $< 200 \text{ m}$ were excluded from the OBE data set because large positioning errors are expected at this offset range. The synthetic data frequencies were selected as 0.125 Hz , 0.375 Hz , and 0.625 Hz based on our measured field data example (Ishizu et al., 2022). The limited frequency range was due to our system design, which was developed for direct-current resistivity surveys. The \log_{10} -scaled E_y amplitudes were used as data inputs of the inversion code (Wheelock et al., 2015).

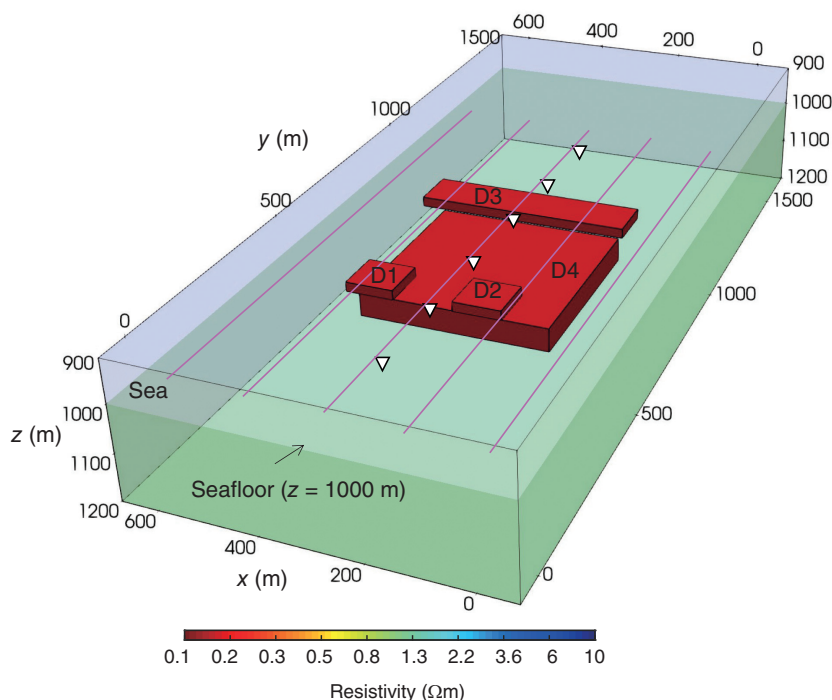


Figure 2. Synthetic model containing three massive sulfide deposits (D1–D3) of $0.2 \Omega\text{m}$ exposed on the seafloor and an embedded massive sulfide deposit (D4) at a depth of 50 mbsf . These massive sulfide deposits are embedded into a $1 \Omega\text{m}$ subsurface layer. Here, z represents the depth from the sea surface. Magenta lines and white triangles represent MEMSYS towing lines at $z = 980 \text{ m}$ and OBE receivers at $z = 1000 \text{ m}$, respectively.

Data were generated by forward modeling using the synthetic model. The resistivity model was discretized using a $59 \times 95 \times 72$ mesh design, and vertical meshes of 7, 14, and 51 were used for the air, sea, and subseafloor regions, respectively. We used a 25 m mesh for the horizontal direction. The electric fields rapidly changed near the transmitter; therefore, we used the finest mesh of 5 m near the transmitter for the vertical direction. With increasing distance to the transmitter, the size of the vertical mesh increases. The starting and prior models for the inversion tests consisted of air ($10^8 \Omega\text{m}$), seawater ($0.3 \Omega\text{m}$), and homogeneous background layers ($1 \Omega\text{m}$). Resistivity values of air and sea layers were fixed during the inversion process. The number of unknown model parameters M is 97,440.

The synthetic OBE data with $N_{\text{OBE}} = 1965$ were superimposed with Gaussian random noise. The noise levels depended on the transmitter-receiver offset and were 6%, 5%, 8%, and 13% for the transmitter-receiver separations of <500 m, 500–1000 m, 1000–1500 m, and >1500 m, respectively. The noise levels are based on our field data example reported by Ishizu et al. (2022). The noise level was higher for <500 m separations than for 500–1000 m separations, due to high positioning uncertainty. The towed receiver data with $N_{\text{TOWED}} = 2625$ were superimposed by 3% Gaussian random noise. The combined OBE and towed receiver data yielded a total of $N = 4590$ data points. The error bars for the inversion analysis were set at the level of added noise.

Study area and CSEM field data set

Ieyama hydrothermal area

The Ieyama hydrothermal area is located in the mid-Okinawa Trough in southwest Japan (Figure 3a). The Okinawa Trough is a back-arc basin formed by the Ryukyu subduction zone (Sibuet et al., 1987; Arai et al., 2017). More than 10 hydrothermally active

areas have been documented in the mid-Okinawa Trough (Ishibashi et al., 2015). The Ieyama area was recently discovered in a survey conducted to narrow down the prospective areas of massive sulfide deposits in the mid-Okinawa Trough (Kasaya et al., 2020).

Several studies have reported the occurrences of seafloor and embedded massive sulfides in the Ieyama area (Kasaya et al., 2020; Ishibashi et al., 2022). Kasaya et al. (2020) identify mound structures in this area based on microtopography obtained using an AUV-based multibeam echosounder system (Figure 3b). Mound structures in hydrothermal areas typically contain sulfide minerals (Gehrmann et al., 2019), suggesting the occurrence of seafloor massive sulfides. Furthermore, scientific drilling was performed by Research and Development Partnership for Next Generation Technology of Marine Resources Survey in 2018 and cores were recovered from three sites (Ishibashi et al., 2022). Site UCB1-4-1 drilled up to 70.7 mbsf (shown by the pink square in Figure 3b) has identified sulfide and sulfate minerals at depths of 53–67 mbsf (Ishibashi et al., 2022), indicating the occurrence of embedded massive sulfides. The sulfide mineral group is primarily sphalerite, galena, and pyrite, with minor amounts of chalcopyrite and tennantite (Ishibashi et al., 2022). Kasaya et al. (2020) observe a self-potential (SP) anomaly in this area, which was attributed to the presence of massive sulfides (Figure 3b). Ishizu et al. (2022) obtain a 3D resistivity model for this area by inverting the CSEM data recorded by OBE receivers and find low-resistivity zones that possibly correspond to seafloor and embedded massive sulfides. Here, we improved the resistivity model in the Ieyama area by adding towed receiver data to the OBE data.

CSEM field data set

Our CSEM data set consists of the towed receiver data that were newly analyzed in this study and the OBE receiver data previously presented by Ishizu et al. (2022). Note that the towed receiver data

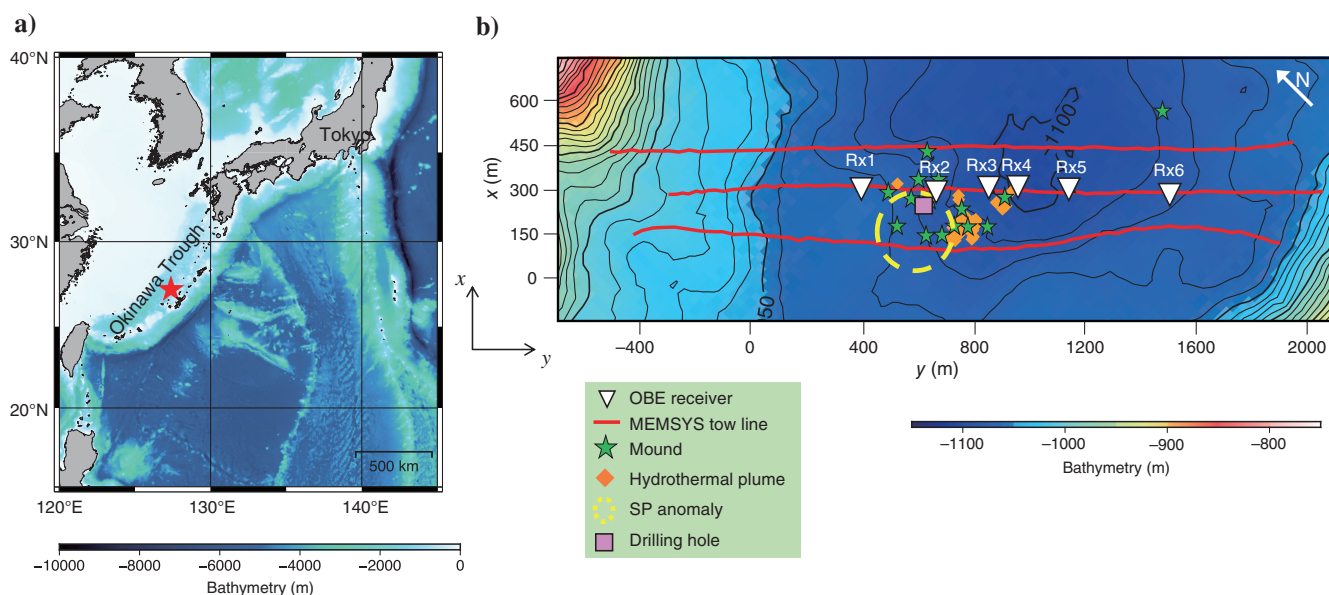
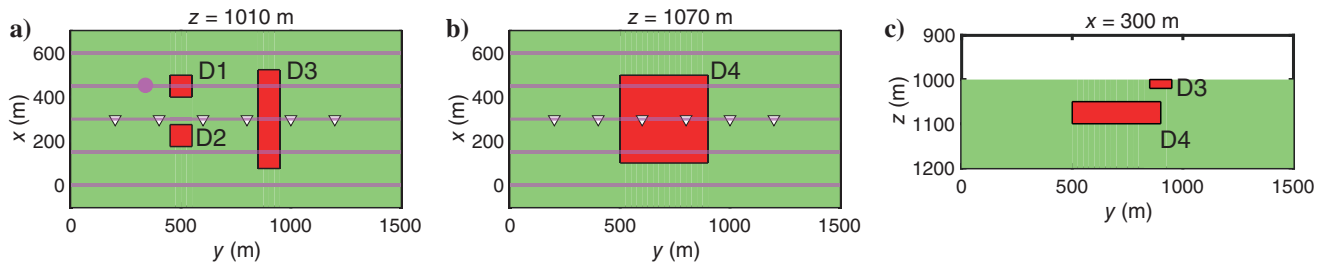


Figure 3. (a) Location of the Ieyama hydrothermal field (red star), off Okinawa, modified from Ishizu et al. (2022). (b) Bathymetric map of the Ieyama hydrothermal field modified from Ishizu et al. (2022). White triangles and red curves represent OBE receivers and MEMSYS tow lines, respectively. Mound structures (green stars), hydrothermal plumes (orange squares), and the SP anomaly (yellow dashed circle) identified in this area are shown (Kasaya et al., 2020). The pink square shows the drilling site of UCB1-4-1, which identified sulfide and sulfate minerals (Ishibashi et al., 2022). Note that the original coordinates are rotated counterclockwise by 45° .

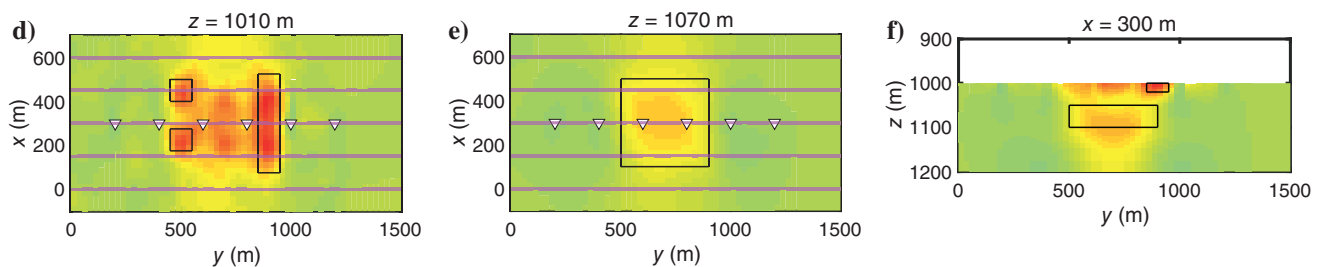
were obtained simultaneously with the OBE data during the KM17-10 cruise survey. We rotated the original horizontal coordinates counterclockwise by 45° for an efficient mesh design of the survey

area using the finite-difference method (Figure 3b), whereas the coordinates were not rotated by Ishizu et al. (2022), thus differentiating this study from Ishizu et al. (2022).

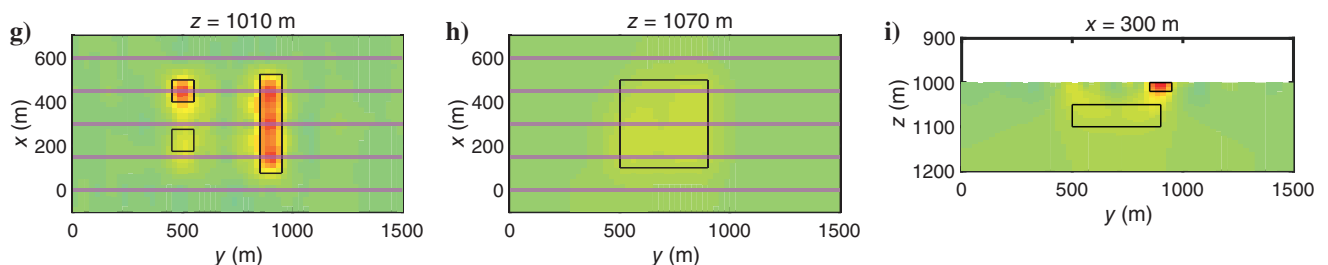
True model



OBE data



Towed data



Combined OBE and towed data

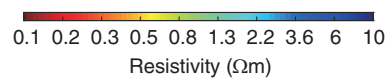
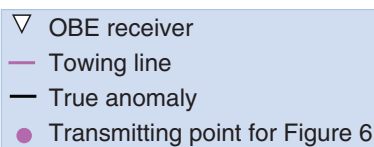
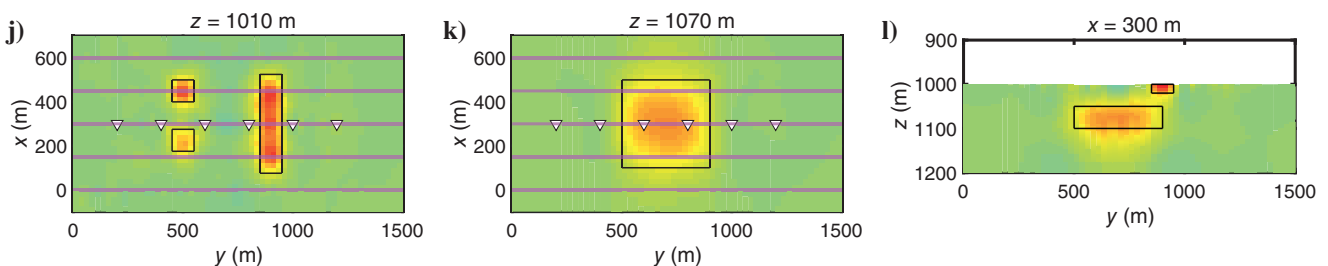


Figure 4. Comparison of the inversion results of the three synthetic data sets. Cross sections of the true resistivity model at (a) $z = 1010$ m, (b) $z = 1070$ m, and (c) $x = 300$ m. Inverted models using (d–f) OBE data alone, (g–i) towed data alone, and (j–l) combined OBE and towed data are shown. The vertical direction is shown with a 2:1 exaggeration. The white triangles and magenta lines mark the OBE receivers and MEMSYS towing lines, respectively. The black lines show the outlines of the true anomaly. The magenta dot shown in (a) is a transmitting point for the data shown in Figure 6.

Our towing system, MEMSYS, repeatedly transmitted electric currents with a towing speed of 1.3 knots (Ishizu et al., 2022). The electric current waveforms consist of 2 s of +60 A (zero to peak), 2 s off, 2 s of -60 A (zero to peak), and 14 s off (Ishizu et al., 2022). The procedure for analyzing the towed receiver data is similar to that used for the OBE data by Ishizu et al. (2022). Time series voltage data at the towed receivers were transformed to the frequency domain by fast Fourier transform over an 8 s window length. Then, the data were stacked with a window of 68 s, which corresponds to 45 m with the horizontal movement of MEMSYS (Ishizu et al., 2022). We obtained the inline electric field data (E_y) for the seven electrode pairs of MEMSYS by dividing the stacked voltage data by the receiver dipole lengths. Only the data from four electrode pairs, ch1–ch2, ch2–ch3, ch3–ch4, and ch4–ch5, were used because of the poor data quality in the other pairs. The E_y amplitude data at three frequencies 0.125 Hz, 0.375 Hz, and 0.625 Hz were used for the towed data inversion analysis. The combined number of available data points for the towed receivers accumulated to 1116 ($N_{\text{TOWED}} = 1116$). The positions of MEMSYS and the cable tail were monitored using attached acoustic transponders with a supershort baseline acoustic navigation system (Ishizu et al., 2022). The towed altitude of MEMSYS was mostly kept at approximately 20 m above the seafloor except at the ends of the survey lines (<60 m) using an attached acoustic altimeter (Ishizu et al., 2022).

The time-series voltage data at six OBE receivers were analyzed by Ishizu et al. (2022). The analyzed OBE data consist of amplitudes of the horizontal electric field at three frequencies: 0.125 Hz, 0.375 Hz, and 0.625 Hz (Ishizu et al., 2022). We converted the electric field data in Ishizu et al. (2022) to E_x and E_y , corresponding to the coordinates defined by the counterclockwise 45° rotation. We excluded noisy data with errors (e) of >50% and data with a transmitter-receiver offset of <150 m owing to large positioning errors. Therefore, the transmitter-receiver separations for the OBE receiver data were 150–2000 m, and OBE data with $N_{\text{OBE}} = 3365$ were used in the inversion. Additional details on the OBE receiver data analysis are described in Ishizu et al. (2022).

RESULTS AND DISCUSSION

Synthetic modeling study

Inversion of OBE data only

Synthetic OBE receiver data generated from a resistivity model (Figures 2 and 4a–4c) are inverted. The inversion yields a minimum norm model with an rms misfit of 1.0 after three iterations, whereas the rms misfit of the starting model is 2.1. The inversion recovers seafloor massive sulfides of D1–D3 (Figure 4d–4f), with resistivity values close to the true resistivity value of 0.2 Ωm . The inversion also recovers embedded massive sulfides of D4; however, it appears thicker ($z = 1060$ – 1160 m) than the true model ($z = 1050$ – 1100 m) with a more resistive peak value of 0.47 Ωm at $z = 1070$ m compared to the true resistivity of 0.2 Ωm (Figure 5). The discrepancy between the initial model response and the observed E_y amplitudes is due to D1–D4 (Figure 6). Thus, the discrepancy indicates the sensitivity of the CSEM data to D1–D4. For the transmitting point (x, y, z) = (450 m, 350 m, 980 m), the discrepancy for the receiver at $y = 600$ m is primarily due to D1 and D2, whereas $y = 1200$ m is primarily due to D1, D3, and D4. The recovery of D1–D4 is consistent with the data sensitivity. Although OBE data are capable of imaging all the conductive anomalies of D1–D4, shallow conductive

artifacts of 0.35–0.45 Ωm appear in the resistivity model between D1 and D3 due to a lack of short transmitter-receiver separation data to constrain shallow structures (Figure 4d). This indicates that the OBE data are sensitive to D1–D4, yet the inversion results can be improved by combining towed data with the OBE data. The recovered model with the conductor artifacts (Figure 4d–4f) also explains the observed data (Figure 6) because of the nonuniqueness of EM data inversion (Constable et al., 1987; Commer and Newman, 2009; Zhdanov, 2010).

Inversion of towed receiver data only

The inversion of synthetic towed receiver data yields a minimum norm model with an rms misfit of 1.0 after two iterations for which

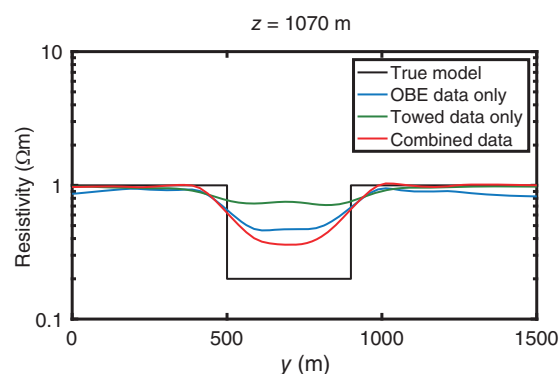


Figure 5. Line plot of models at $z = 1070$ m along the y -axis at $x = 300$ m. The black, blue, green, and red lines correspond to the true model, inversion results of OBE receiver data alone, towed receiver data alone, and combined OBE and towed receiver data, respectively.

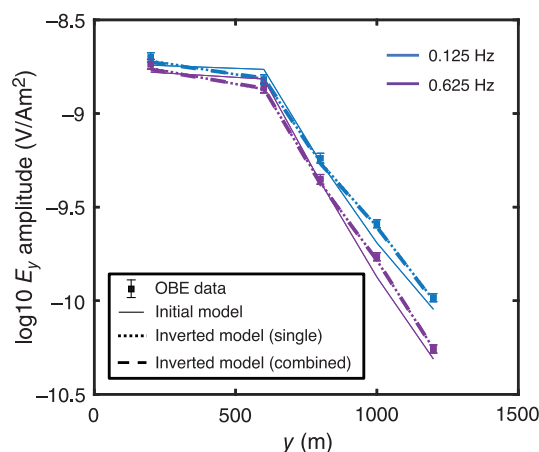


Figure 6. Observed and predicted E_y amplitudes (V/Am^2) for the OBE-only data set and the combined data set. The data represent the response received by the OBE receivers from a transmitting point (x, y, z) = (450 m, 350 m, 980 m), shown as a magenta dot in Figure 4a. The data are plotted at the receiver positions projected to the y -axis. Dots with error bars, thin solid lines, dotted lines, and dashed lines indicate observed data, predicted data by the initial model, predicted data by the final model of the single-type receiver data, and predicted data by the final model of the combined data, respectively. Blue and purple colors correspond to the frequencies of 0.125 Hz and 0.625 Hz, respectively. The initial model consists of three layers: a resistive air layer ($10^8 \Omega\text{m}$), a sea layer (0.3 Ωm), and a homogeneous subsurface layer (1 Ωm).

the initial rms misfit is 2.2. The inversion sufficiently recovers the positions and resistivity values of D1 and D3, which are located directly below the towing lines of $x = 450$ m (Figure 4g–4i). Two V-shaped low-amplitude data anomalies are observed at $y = 500$ m and 700 m, which correspond to the cases in which either the receiver or transmitter is above D1 (Figure 7a). Another two V-shaped amplitude anomalies are observed at $y = 900$ m and 1100 m, which correspond to the cases in which either the receiver or transmitter is above D3 (Figure 7a). The sufficient recovery of D1 and D3 is consistent with the high sensitivity of the data along the towing line of $x = 450$ m to D1 and D3 (Figure 7a). The inversion poorly images D2, which are located between the towing lines. The poor recovery of D2 can be explained by the weak sensitivity of the data to D2 due to the absence of towed data directly above D2. Even the data for the towline at $x = 150$ m, closest to D2, show weak sensitivity to D2 (Figure 7b). The high-recovery feature for structures directly below the towing line and the low-recovery feature for structures between the towing lines are consistent with the inversion

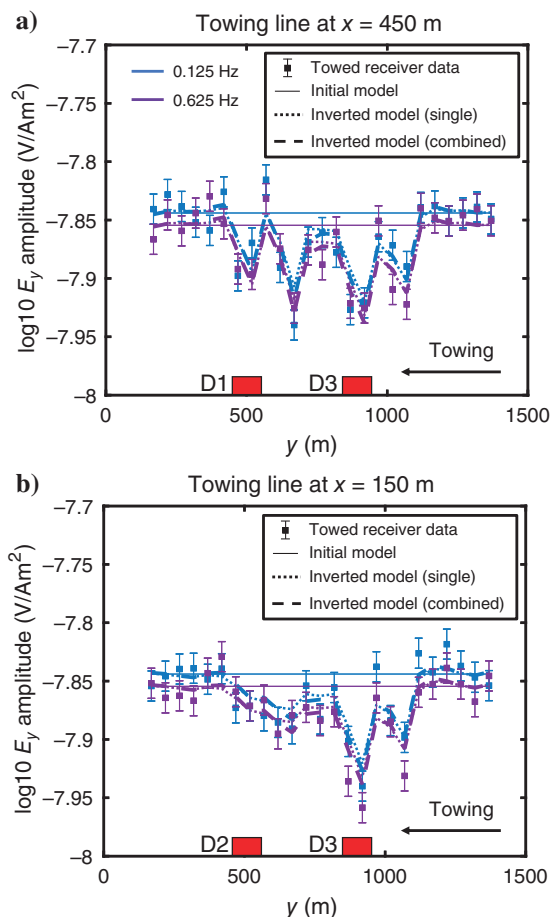


Figure 7. Observed and predicted E_y amplitudes (V/Am^2) of the towed receiver for the towed receiver-only data set and the combined data set. The E_y amplitudes at the towing line (a) $x = 450$ m and (b) $x = 150$ m are shown. The E_y data are shown for the ch7–ch8 electrode pair of MEMSYS at an offset of 169 m behind the transmitter and plotted at the receiver positions projected to the y -axis (the transmitter position is the receiver position minus 169 m). The towing is from right to left in the figure. The red rectangles indicate a horizontal position of D1–D3. Other explanations are the same as in Figure 6.

results of Morten et al. (2016) for the hydrocarbon model. The inversion of the towed data also does not image D4 owing to the limited investigation depth of the towed data. The similarity of the E_y amplitudes of the three frequency bands indicates that inductive attenuation is not evident in these frequency bands (Figure 7). Higher frequency data, such as 5 Hz, include inductive attenuation (Gehrmann et al., 2020); therefore, adding it may improve the inversion resolution. Poor data fitting is observed at points where E_y amplitudes increase rapidly, such as at $y = 600$ m (Figure 7a) and $y = 1000$ m (Figure 7b). We attribute the poor fitting to the smoothing effect in the inversion.

Combined inversion of OBE and towed receiver data

The combined inversion of OBE and towed receiver data results in an initial rms misfit of 2.1 and recovers a minimum norm model with an rms misfit of 1.0 after four iterations. Unlike the inversion model using solely OBE data, the combined inversion of towed and OBE data resolves D1–D3 without any conductive artifacts (Figure 4j). In addition, the combined inversion resolves D4 better than the inversions of the single-type receiver data (Figure 4k and 4l). For recovered D4 at $z = 1070$ m, the peak resistivity values are $0.36 \Omega\text{m}$ and $0.47 \Omega\text{m}$ for the combined data set and OBE-only data set, respectively (Figure 5). This indicates that the conductive artifacts by the OBE-only inversion deteriorate the imaging of the deep structures, whereas the combined inversion improves the imaging of the embedded massive sulfides while recovering the shallow resistivity structures more accurately. We inverted the combined data with different initial models of $0.5 \Omega\text{m}$ and $1.5 \Omega\text{m}$ to investigate their influence on inversion results. The inversion with the initial models also produces the minimum norm models with an rms misfit of 1.0 after four iterations and maps D1–D4 without conductive artifacts, confirming the minor influence of the initial models on the inversion results.

The data fitting for the single (dotted line) and combined data sets (dashed line) are identical for the OBE data (Figure 6), the same for the towed data at 0.625 Hz, and very similar for the towed data at 0.125 Hz (Figure 7). For this synthetic data example, the combined inversion mitigates the nonuniqueness issues (Commer and Newman, 2009) and improves the CSEM resistivity imaging of seafloor and embedded massive sulfides by supplementing the low-sensitivity zone of each data set. The presented CSEM application is capable of providing detailed maps of seafloor and embedded massive sulfides, which are necessary for their accurate resource assessment.

Inversion of field data in the Ieyama area

We obtained 3D subsurface resistivity models for the Ieyama area by inverting the measured CSEM data sets (the OBE receiver data set, the towed receiver data set, and the combined OBE and towed receiver data set). Air, sea, and subsurface regions are discretized using a $62 \times 99 \times 75$ mesh. We use a 30 m mesh for the horizontal directions and a vertical mesh of 5 m for depths between 1000 m and 1120 m below the sea surface to represent the seafloor topography. The sea region consists of five laterally stratified seawater layers ($0.2\text{--}0.3 \Omega\text{m}$), and the resistivity values of the sea layers are estimated based on the measured values by the conductivity-temperature-depth sensor mounted on MEMSYS (Ishizu et al., 2022). The starting and prior models consist of a $10^8 \Omega\text{m}$ air

layer, five seawater layers, and a 1 Ωm subseafloor layer. The model resistivity values of the air and sea regions are fixed during the inversion. We apply a minimum error of 5% to the OBE data to prevent overfitting against systematic noise (Ishizu et al., 2022). A minimum error of 3% is applied to the towed data.

The inversion of the OBE receiver data alone yields a resistivity model with an rms misfit of 1.44 after six iterations (Figure 8a). Although conducting more than six iterations yields a model with a slightly smaller rms misfit than 1.44, the roughness of the model increases. Due to the balance between the reduction of rms misfit and the increase of model roughness, we select the model with the rms misfit of 1.44 for interpretation. We also use the criteria that consider the balance between the reduction of misfit and the increase of model roughness for model selection of the inversion result of the individual towed receiver data and combined data.

The obtained OBE resistivity model is slightly different from that of Ishizu et al. (2022) because of the use of different mesh designs and coordinates, although their main features are similar. The recovered resistivity model identifies several conductive zones. Conductors of CD1a, CD6a, and CD3a of 0.2–0.4 Ωm extend from the seafloor to $z = 1300$ m below the mound and SP anomaly zones ($500\text{ m} < y < 750\text{ m}$). A buried conductor CD4a of 0.1–0.2 Ωm and 45–60 m thickness is found with its top at a depth of 15 mbsf ($850\text{ m} < y < 1000\text{ m}$). Elongated conductors CD2a and CD5a of 0.2–0.3 Ωm and 10–30 m thickness are present near the seafloor ($70\text{ m} < y < 400\text{ m}$ and $1000\text{ m} < y < 1450\text{ m}$, respectively). Responses from the recovered resistivity model fit the observed OBE data (Figure 9a).

The inversion of the towed receiver data alone yields a resistivity model with an rms misfit of 1.49 after seven iterations (Figure 8b), and responses from the resistivity model fit the observed towed data (Figure 9b). The resistivity model mainly consists of three layers: a low-resistivity layer of 0.1–0.3 Ωm with 10–30 m thickness near the seafloor, a 0.8–1.5 Ωm layer with 20–30 m thickness below the first layer, and a 1.5–3.5 Ωm layer below the second layer. Features of the first layer are consistent with the elongated conductors near the seafloor in the OBE data model; however, the $y = 500$ m and $y = 850$ m conductive layers near the seafloor are not found in the OBE data model. The model differences are caused by the sensitivity difference between the OBE and towed receiver data sets, as suggested by our synthetic data example.

The OBE and towed receiver data sets are inverted together to improve the CSEM resistivity imaging of massive sulfides. The inversion recovers a resistivity model with an rms misfit of 1.57 after six iterations (Figure 8c). The obtained resistivity model also explains the observed OBE and towed receiver data (Figure 9a and 9b). Although this model is broadly consistent with the models derived using individual receiver data sets, there is a significant difference in the resistivity structures

below Rx2. Here, CD6a in the OBE data model disappears in the combined inversion model, whereas CD1 and CD3 are imaged in the combined data model.

The sulfide and sulfate mineralization in this area was assessed by seafloor drilling down to 70.7 m and recognized in the sediment at 53–67 mbsf (Ishibashi et al., 2022). Figure 10a and 10b shows the resistivity profile of the combined and single inversion models at the location of the borehole and a depth section of core lithology from the borehole, respectively. The mineralization zone coincides with the top of CD1 ((x, y, z) : $0\text{ m} < x < 350\text{ m}$, $450\text{ m} < y < 750\text{ m}$, and $1140\text{ m} < z < 1350\text{ m}$) in the combined inversion model (Figures 8c, 10a, and 11). Therefore, CD1 can be interpreted as embedded massive sulfides. Sampled sediment analysis (Ishibashi et al., 2022) suggests that CD1 includes sphalerite, galena, and pyrite, with minor amounts of chalcopyrite and tennantite. The positional coincidence of CD1 and an SP anomaly (Kasaya et al., 2020) suggests that CD1 mainly contributes to the SP anomaly. Here, CD6a in the OBE data model suggests a mineralization zone extending from the seafloor to 60 mbsf, yet the drilling did not find such a mineralization

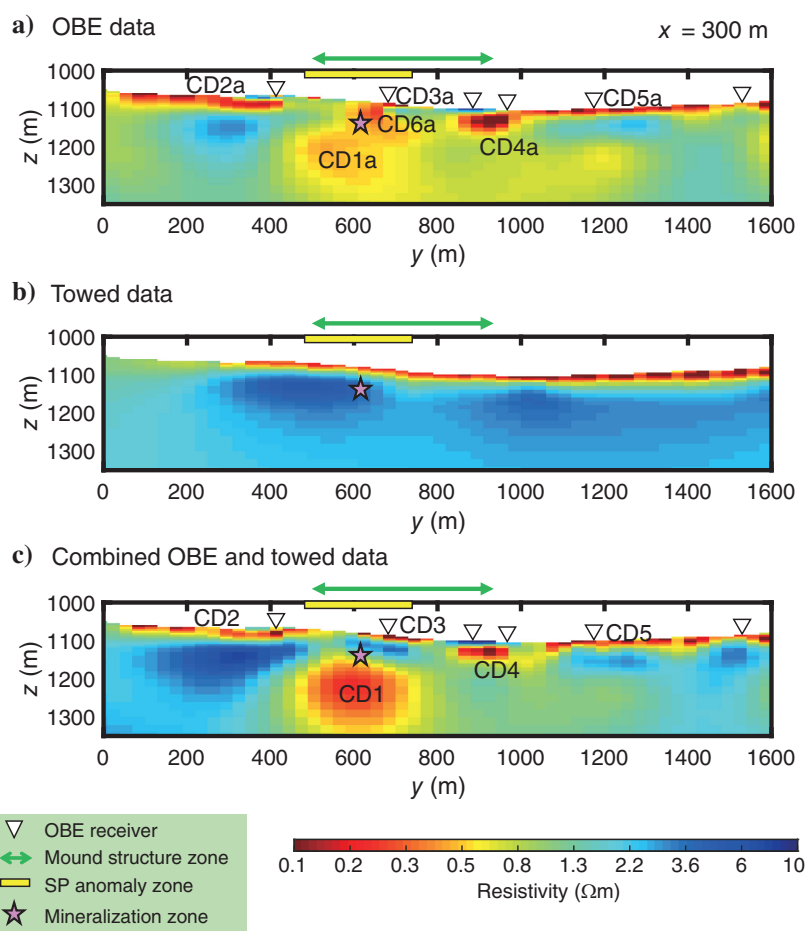


Figure 8. Comparison of the inversion results of measured data from the Ieyama area. (a–c) The vertical cross sections of the inverted models at $x = 300$ m using the OBE data alone, towed data alone, and combined OBE and towed data, respectively. The pink star displays a zone of sulfide and sulfate minerals at depths of 53–67 mbsf, identified by scientific drilling (Ishibashi et al., 2022). The yellow rectangle and green arrow indicate the locations where the SP anomalies and mound structures were identified, respectively (Kasaya et al., 2020). Designations CD1a–CD6a and CD1–CD5 denote subseafloor conductive zones.

zone. Therefore, we conclude that CD6a is an artifact of the OBE inversion. Given that the combined inversion specifies the mineralization identified in the drilling as CD1 and the artifact in the OBE data model disappears in the combined inversion model, we conclude that combined inversion delineates a resistivity structure in the Ieyama hydrothermal area more precisely than individual data set inversion.

Near-seafloor conductors of CD2, CD3, CD4, and CD5 are possibly related to seafloor and embedded massive sulfides. Kasaya et al. (2020) find mound structures on the seafloor above CD3 (Figure 8c). Because mound structures in hydrothermal areas frequently contain sulfide minerals (Petersen et al., 2000; Gehrman et al., 2019), we interpret CD3 as seafloor massive sulfides. The disappearance of artifact CD6a below CD3 in the combined inversion model leads to improved accuracy in delineating the vertical spatial extent of CD3. Here, CD4 is found with its top at a depth of 15 mbsf; thus, we interpret CD4 as embedded massive sulfides.

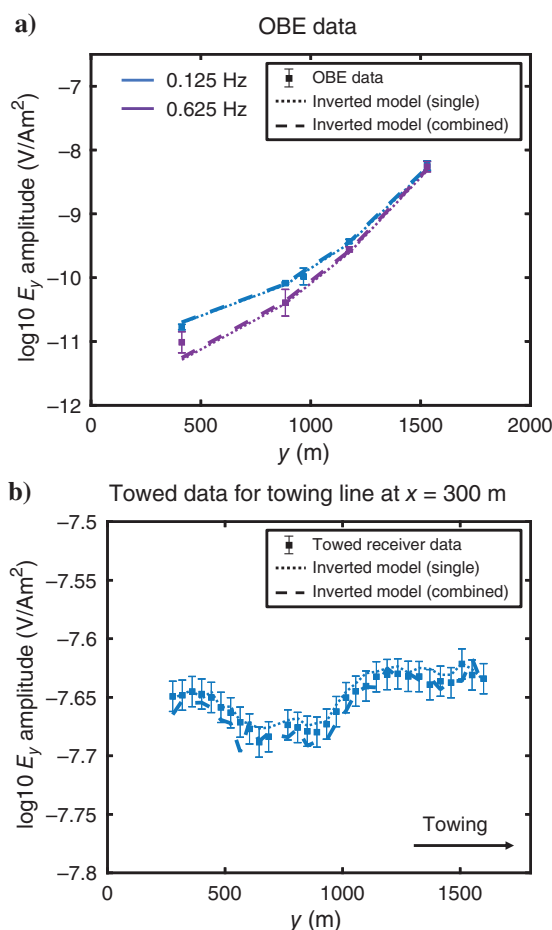


Figure 9. Observed and predicted E_y amplitudes (V/Am^2) for the Ieyama area. (a) The OBE data are plotted for a transmitting point $(x, y, z) = (292 \text{ m}, 1784 \text{ m}, 1058 \text{ m})$ and frequencies of 0.125 Hz and 0.625 Hz. The Rx2 data points resulting from this transmitting point are not shown because the data are excluded from the inversion analysis due to its large error. (b) The 0.125 Hz towed data are shown for the ch4–ch5 electrode pair of MEMSYS with the offset 139 m at the towing line $x = 300 \text{ m}$ and plotted at receiver positions. The towing is from left to right in the figure. Other explanations are the same as in Figure 6.

At CD4, the AUV survey did not detect SP data anomalies (Kasaya et al., 2020). We attribute this to the high towing altitude of the AUV survey (approximately 70 m). The size of CD4 is too small to detect SP anomalies for an AUV survey with a high altitude. Altitude effects on SP anomaly detection are discussed in Kawada and Kasaya (2017). In contrast, CD1 is detected as an SP anomaly even at high altitudes due to its large size. Hydrothermal plumes are observed above CD3 and CD4 (Kasaya et al., 2020), indicating their formation is related to current hydrothermal activity. Mound structures are not observed above CD2 and CD5, and the mineralization zones in CD2 and CD5 may have been buried below the seafloor by sedimentation (Ishizu et al., 2022).

Implications for mineral potential and effective survey design

The synthetic modeling result demonstrates that the resistivity models generated by the inversion of individual receiver data sets lead to overestimation or underestimation of the mineral potential, but the combined inversion recovers a resistivity model allowing proper estimation of the mineral potential. The inversion of OBE data recovers seafloor and embedded massive sulfides but additionally includes conductive artifacts, which can lead to overestimates of the mineral potential (Figure 4d–4f). The inversion of towed data recovers seafloor massive sulfides below the towing lines yet does not recover embedded massive sulfides and seafloor massive sulfides between the towing lines, which causes underestimates of the mineral potential (Figure 4g–4i). In the combined inversion approach, the towed data constrain the OBE data resulting in more accurate delineation of seafloor and embedded massive sulfides without additional artifacts (Figure 4j–4l). Therefore, the combined inversion approach can contribute to a more accurate estimation of the mineral potential and the decision of future drilling points.

The combined inversion of measured CSEM data in the Ieyama area eliminates a prominent artifact (CD6a) in the OBE model by adding towed data to the OBE data, resulting in the delineation of embedded massive sulfides as CD1 (Figures 8 and 10a). Ishizu et al. (2022) estimate mineral potential in the Ieyama area using the OBE model. The OBE model contains the artifact (CD6a) and poorly recovers the embedded massive sulfides (CD1). The towed model does not delineate the embedded massive sulfides (Figures 8b and 10a). Thus, the mineral potential estimation based on the OBE and towed models contains large errors. In the combined inversion approach, the towed data constrain the OBE data at shallow depths resulting in delineation of the embedded massive sulfides without the artifact, allowing for a more accurate estimation of the mineral potential in the Ieyama area.

The combined inversion approach is useful for reducing the uncertainties involved in previous predictions of mineral potential. Graber et al. (2020) delineate outlines of mounds using high-resolution bathymetric data in the Trans-Atlantic Geotraverse hydrothermal field and assess the mineral potential of seafloor massive sulfide deposits assuming that mineralized materials were uniformly distributed in the mounds. However, due to insufficient information on the distribution of massive sulfide deposits, the estimation of the vertical extent of the mineralized zone involved a large uncertainty. Moreover, embedded massive sulfide deposits were not included in the mineral potential estimation. Therefore, large uncertainty is involved in their estimation of mineral potential. The combined inversion can accurately delineate the distribution of seafloor and

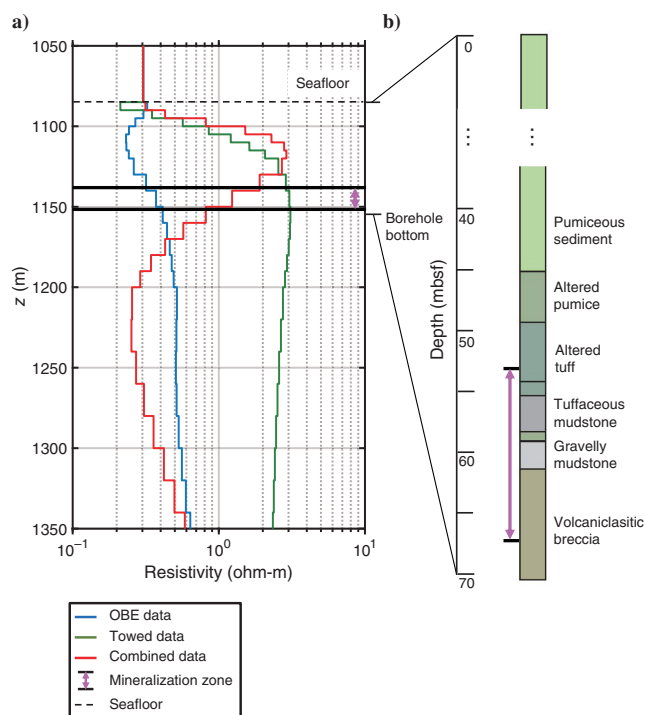


Figure 10. Comparison of inverted models of measured data with borehole core lithology. (a) Vertical depth profile of the inverted models at the location of the borehole UCB1-4-1 shown in Figure 3b. Blue, green, and red lines show the inverted models using the OBE data alone, towed data alone, and combined OBE and towed data, respectively. The black lines with a magenta arrow indicate a zone of sulfide and sulfate minerals at depths of 53–67 mbsf (Ishibashi et al., 2022). (b) Geologic column showing core lithology from the borehole UCB1-4-1, modified from Ishibashi et al. (2022).

embedded massive sulfide deposits, thereby reducing the uncertainties involved in previous predictions of mineral potential.

Our synthetic modeling study also provides an insight into an optimal CSEM survey design. To map the massive sulfide deposits using towed data only, the towing line should cross directly over the deposits (Figure 4g–4i). This is because the towed data are highly sensitive to structures below the towing line but less sensitive to structures at a distance from the towing line (Figure 7b). If the location of the target massive sulfides is unavailable prior to a CSEM survey and only towed data are used, a survey with a dense towing grid, which can cross directly over them, is considered ideal for mapping the unknown massive sulfides. However, the CSEM survey requires a longer ship time. In contrast, the combined inversion of OBE and towed receiver data can delineate the massive sulfides even if the towing line does not necessarily pass directly over them (Figure 4j–4l). The combined inversion also is useful for delineating embedded massive sulfides. Therefore, the CSEM survey using two receiver types is an optimal CSEM survey for massive sulfide deposits. Although this study considers a specific measurement setup using OBE receivers placed on a line and a towing system with short transmitter-receiver offsets, the concept of integrating towed receiver data with OBE data into a 3D inversion framework also is beneficial to other CSEM surveys using various measurement setups.

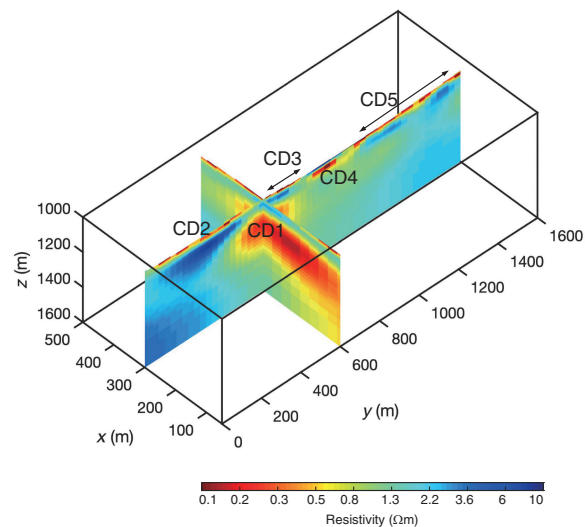


Figure 11. Fence plot of the resistivity model obtained by the combined inversion of OBE and towed data for the Ieyama area. The two vertical cross sections of the resistivity model at $x = 300$ m and $y = 600$ m are shown. Note that the vertical cross section of the resistivity model at $x = 300$ m is already shown in Figure 8c.

CONCLUSION

This study presents a CSEM framework using a towed electric dipole transmitter and two receiver types, stationary OBE and short-offset towed, to distinguish and map seafloor and embedded massive sulfides. An example using synthetic data demonstrates that the combined inversion of OBE and towed receiver data can recover resistivities and positions of the massive sulfides more accurately than individual receiver inversions. The inversion of the towed receiver-only data set recovers seafloor massive sulfides located below the towing line. However, it does not recover seafloor massive sulfides located between the towing lines and the embedded massive sulfides, which causes underestimates of the mineral potential. Our synthetic modeling study also indicates that the towing line should cross directly over the seafloor massive sulfides to map them using only towed data. The inversion of OBE receiver-only data recovers seafloor massive sulfides located below and between the towing lines and embedded massive sulfides; however, near-seafloor conductive artifacts also are imaged between seafloor massive sulfides and the shape of recovered embedded massive sulfides is substantially different from the true shape. The conductive artifacts in the OBE model inevitably lead to overestimates of the mineral potential. In contrast, the combined inversion can map surface seafloor massive sulfides located below and between the towing lines without the artifacts. The combined inversion also recovers the shape and resistivities of embedded massive sulfides more precisely than the inversions of individual receiver data sets. The combined inversion improves resistivity imaging of the massive sulfides by supplementing the low-sensitivity zone of each data set. The resistivity model derived using the combined inversion approach can increase the estimation accuracy of the mineral potential of massive sulfide deposits.

Subsequently, we performed the combined inversion of CSEM data obtained from the Ieyama hydrothermal area of the Okinawa Trough. The combined inversion recovers a buried conductor of

CD1, and a top depth of CD1 is positionally coincidental with the mineralization zone identified by drill cores. Based on its positional coincidence, we interpret CD1 as embedded massive sulfides. The towed data inversion does not recover the embedded massive sulfides, and the OBE data inversion not only specifies them but also images a conductive artifact above it. The combined inversion eliminates the artifact in the OBE model by adding towed data to the OBE data, resulting in the delineation of embedded massive sulfides of CD1 and mound massive sulfides of CD3. Given that the combined inversion maps embedded massive sulfides identified by drilling as CD1 and the artifact in the OBE model disappears, we conclude that combined inversion delineates a resistivity structure in the Ieyama hydrothermal area more precisely than individual data set inversion. Delineation of the embedded massive sulfides without the artifact by the combined inversion revises the previous estimation of the mineral potential derived using the OBE model.

ACKNOWLEDGMENTS

We would like to thank A. Haroon, M. Jegen, an anonymous reviewer, and the editors for their detailed and valuable comments that led to significant improvements in this paper. We thank the captain, crew, and technicians of the KM17-10 cruise survey for assisting the field operation. This work was supported by the Japan Society for the Promotion of Science KAKENHI (grant nos. 17J08764 and 22K14104) and the Cross-ministerial Strategic Innovation Promotion Program “Next Generation Technology for Ocean Resources Exploration.”

DATA AND MATERIALS AVAILABILITY

Synthetic data associated with this research are available and can be provided by contacting the corresponding author. Field data are confidential and cannot be released.

REFERENCES

- Arai, R., S. Kodaira, K. Yuka, T. Takahashi, S. Miura, and Y. Kaneda, 2017, Crustal structure of the southern Okinawa Trough: Symmetrical rifting, submarine volcano, and potential mantle accretion in the continental back-arc basin: *Journal of Geophysical Research: Solid Earth*, **122**, 622–641, doi: [10.1002/2016JB013448](https://doi.org/10.1002/2016JB013448).
- Attias, E., K. Weitmeyer, S. Hölz, S. Naif, T. A. Minshull, A. I. Best, A. Haroon, M. Jegen-Kulcsar, and C. Berndt, 2018, High-resolution resistivity imaging of marine gas hydrate structures by combined inversion of CSEM towed and ocean-bottom receiver data: *Geophysical Journal International*, **214**, 1701–1714, doi: [10.1093/gji/ggy227](https://doi.org/10.1093/gji/ggy227).
- Boschen, R. E., A. A. Rowden, M. R. Clark, and J. P. Gardner, 2013, Mining of deep-sea seafloor massive sulfides: A review of the deposits, their benthic communities, impacts from mining, regulatory frameworks and management strategies: *Ocean & Coastal Management*, **84**, 54–67, doi: [10.1016/j.ocecoaman.2013.07.005](https://doi.org/10.1016/j.ocecoaman.2013.07.005).
- Cairns, G. W., R. L. Evans, and R. N. Edwards, 1996, A time domain electromagnetic survey of the TAG hydrothermal mound: *Geophysical Research Letters*, **23**, 3455–3458, doi: [10.1029/96GL03233](https://doi.org/10.1029/96GL03233).
- Commer, M., and G. A. Newman, 2009, Three-dimensional controlled-source electromagnetic and magnetotelluric joint inversion: *Geophysical Journal International*, **178**, 1305–1316, doi: [10.1111/j.1365-246X.2009.04216.x](https://doi.org/10.1111/j.1365-246X.2009.04216.x).
- Constable, S., P. Kowalczyk, and S. Bloomer, 2018, Measuring marine self-potential using an autonomous underwater vehicle: *Geophysical Journal International*, **215**, 49–60, doi: [10.1093/gji/ggy263](https://doi.org/10.1093/gji/ggy263).
- Constable, S. C., R. L. Parker, and C. G. Constable, 1987, Occam's inversion: A practical algorithm for generating smooth models from electromagnetic sounding data: *Geophysics*, **52**, 289–300, doi: [10.1190/1.1442303](https://doi.org/10.1190/1.1442303).
- Fuchs, S., M. D. Hannington, and S. Petersen, 2019, Divining gold in seafloor polymetallic massive sulfide systems: *Mineralium Deposita*, **54**, 789–820, doi: [10.1007/s00126-019-00895-3](https://doi.org/10.1007/s00126-019-00895-3).
- Gehrmann, R. A. S., A. Haroon, M. Morton, A. T. Djanni, and T. A. Minshull, 2020, Seafloor massive sulphide exploration using deep-towed controlled source electromagnetics: Navigational uncertainties: *Geophysical Journal International*, **220**, 1215–1227, doi: [10.1093/gji/ggz513](https://doi.org/10.1093/gji/ggz513).
- Gehrmann, R. A. S., L. J. North, S. Graber, F. Sztikar, S. Petersen, T. A. Minshull, and B. J. Murton, 2019, Marine mineral exploration with controlled source electromagnetics at the TAG hydrothermal field, 26° N Mid-Atlantic Ridge: *Geophysical Research Letters*, **46**, 5808–5816, doi: [10.1029/2019GL082928](https://doi.org/10.1029/2019GL082928).
- German, C. R., S. Petersen, and M. D. Hannington, 2016, Hydrothermal exploration of mid-ocean ridges: Where might the largest sulfide deposits be forming? *Chemical Geology*, **420**, 114–126, doi: [10.1016/j.chemgeo.2015.11.006](https://doi.org/10.1016/j.chemgeo.2015.11.006).
- Graber, S., S. Petersen, I. Yeo, F. Sztikar, M. Klischies, J. Jamieson, M. Hannington, M. Rothenbeck, E. Wenzlaff, N. Augustin, and I. Stobbs, 2020, Structural control, evolution, and accumulation rates of massive sulfides in the TAG hydrothermal field: *Geochemistry, Geophysics, Geosystems*, **21**, e2020GC009185, doi: [10.1029/2020GC009185](https://doi.org/10.1029/2020GC009185).
- Hannington, M., J. Jamieson, T. Monecke, and S. Petersen, 2010, Modern sea-floor massive sulfides and base metal resources: Toward an estimate of global sea-floor massive sulfide potential, *in* R. J. Goldfarb, E. E. Marsh, and T. Monecke, eds., *The challenge of finding new mineral resources: Global metallogeny, innovative exploration, and new discoveries: Society of Economic Geologists*.
- Hannington, M., J. Jamieson, T. Monecke, S. Petersen, and S. Beaulieu, 2011, The abundance of seafloor massive sulfide deposits: *Geology*, **39**, 1155–1158, doi: [10.1130/G32468.1](https://doi.org/10.1130/G32468.1).
- Haroon, A., S. Hölz, R. A. S. Gehrmann, E. Attias, M. Jegen, T. A. Minshull, and B. J. Murton, 2018, Marine dipole–dipole controlled source electromagnetic and coincident-loop transient electromagnetic experiments to detect seafloor massive sulphides: Effects of three-dimensional bathymetry: *Geophysical Journal International*, **215**, 2156–2171, doi: [10.1093/gji/ggy398](https://doi.org/10.1093/gji/ggy398).
- Hölz, S., and M. Jegen, 2016, How to find buried and inactive seafloor massive sulfides using transient EM — A case study from the Palino Seamount: EAGE/DGG Workshop on Deep Mineral Exploration, doi: [10.3997/2214-4609.201600037](https://doi.org/10.3997/2214-4609.201600037).
- Humphris, S. E., P. M. Herzig, D. J. Miller, J. C. Alt, K. Becker, D. Brown, G. Brägmann, H. Chiba, Y. Fouquet, and J. B. Gemmill, 1995, The internal structure of an active sea-floor massive sulphide deposit: *Nature*, **377**, 713–716, doi: [10.1038/377713a0](https://doi.org/10.1038/377713a0).
- Imamura, N., T. Goto, T. Kasaya, and H. Machiyama, 2018, Robust data processing of noisy marine controlled-source electromagnetic data using independent component analysis: *Exploration Geophysics*, **49**, 21–29, doi: [10.1071/EG17139](https://doi.org/10.1071/EG17139).
- Ishibashi, J., F. Ikegami, T. Tsuji, and T. Urabe, 2015, Hydrothermal activity in the Okinawa Trough back-arc basin: Geological background and hydrothermal mineralization, *in* J. Ishibashi, K. Okino, and M. Sunamura, eds., *Subseafloor biosphere linked to hydrothermal systems: TAIGA concept*: Springer, 337–359.
- Ishibashi, J., S. Totsuka, T. Miyamoto, Y. Itatani, K. Shimada, Y. Okazaki, T. Yamasaki, K. Ikehara, T. Nagase, Y. Takaya, R. Shinjo, T. Yamanaka, K. Arai, M. Tomita, S. Toyoda, H. Machiyama, K. Iijima, H. Yamamoto, and H. Kumagai, 2022, Sulfide and sulfate mineralization within a volcanic conduit located in an active hydrothermal field in the Okinawa Trough: *Proceedings of the 16th SGA Biennial Meeting*, 153–155.
- Ishizu, K., T. Goto, Y. Ohta, T. Kasaya, H. Iwamoto, C. Vachiriatienchai, W. Siripunvaraporn, T. Tsuji, H. Kumagai, and K. Koike, 2019, Internal structure of a seafloor massive sulfide deposit by electrical resistivity tomography, Okinawa Trough: *Geophysical Research Letters*, **46**, 11025–11034, doi: [10.1029/2019GL083749](https://doi.org/10.1029/2019GL083749).
- Ishizu, K., W. Siripunvaraporn, T. Goto, K. Koike, T. Kasaya, and H. Iwamoto, 2022, A cost-effective three-dimensional marine controlled-source electromagnetic survey: Exploring seafloor massive sulfides: *Geophysics*, **87**, no. 4, E219–E241, doi: [10.1190/geo2021-0328.1](https://doi.org/10.1190/geo2021-0328.1).
- Kasaya, T., T. Goto, H. Iwamoto, and Y. Kawada, 2019, Development of multi-purpose electromagnetic survey instruments: 13th SEGJ International Symposium, SEG, Global Meeting Abstracts, 159–161, doi: [10.1190/SEGJ2018-042.1](https://doi.org/10.1190/SEGJ2018-042.1).
- Kasaya, T., J. Kaneko, and H. Iwamoto, 2020, Observation and confirmation based on survey protocol for seafloor massive sulfide deposits using acoustic survey technique and self-potential surveys: *BUTSURI-TANSA (Geophysical Exploration)*, **72**, 42–52, doi: [10.3124/segj.73.42](https://doi.org/10.3124/segj.73.42).
- Kasaya, T., H. Machiyama, K. Kitada, and K. Nakamura, 2015, Trial exploration for hydrothermal activity using acoustic measurements at the North Iheya Knoll: *Geochemical Journal*, **49**, 597–602, doi: [10.2343/geochemj.2.0389](https://doi.org/10.2343/geochemj.2.0389).
- Kawada, Y., and T. Kasaya, 2017, Marine self-potential survey for exploring seafloor hydrothermal ore deposits: *Scientific Reports*, **7**, 13552, doi: [10.1038/s41598-017-13920-0](https://doi.org/10.1038/s41598-017-13920-0).

- Koike, K., O. Yono, V. R. de Sá, S. A. Tomita, T. Nozaki, Y. Takaya, and S. Komori, 2022, Effectiveness of neural kriging for three-dimensional modeling of sparse and strongly biased distribution of geological data with application to seafloor hydrothermal mineralization: *Mathematical Geosciences*, **54**, 1183–1206, doi: [10.1007/s11004-022-10011-3](https://doi.org/10.1007/s11004-022-10011-3).
- Kowalczyk, P., 2008, Geophysical prelude to first exploitation of submarine massive sulphides: *First Break*, **26**, 99–106, doi: [10.3997/1365-2397.26.1293.28613](https://doi.org/10.3997/1365-2397.26.1293.28613).
- Meqbel, N., and O. Ritter, 2015, Joint 3D inversion of multiple electromagnetic datasets: *Geophysical Prospecting*, **63**, 1450–1467, doi: [10.1111/1365-2478.12334](https://doi.org/10.1111/1365-2478.12334).
- Monecke, T., S. Petersen, M. D. Hannington, H. Grant, and I. Samson, 2016, The minor element endowment of modern sea-floor massive sulfides and comparison with deposits hosted in ancient volcanic successions: *Reviews in Economic Geology*, **18**, 245–306, doi: [10.5382/Rev.18.11](https://doi.org/10.5382/Rev.18.11).
- Morozumi, H., K. Watanabe, H. Sakurai, H. Hino, Y. Kado, M. Motoori, and H. Tendo, 2020, Additional information for characteristics of seafloor hydrothermal deposits investigated by JOGMEC: Shigen-Chishitsu, **70**, 113–119.
- Morten, J. P., J.-M. Poudroux, and R. Mittet, 2016, A modeling study of augmenting coarse-grid 3D controlled-source electromagnetics with data from a towed receiver array: *Geophysics*, **81**, no. 1, E33–E42, doi: [10.1190/geo2014-0583.1](https://doi.org/10.1190/geo2014-0583.1).
- Müller, H., K. Schwalenberg, K. Reeck, U. Barckhausen, U. Schwarz-Schampera, C. Hilgenfeldt, and T. von Dobeneck, 2018, Mapping seafloor massive sulfides with the Golden Eye frequency-domain EM profiler: *First Break*, **36**, 61–67, doi: [10.3997/1365-2397.n0127](https://doi.org/10.3997/1365-2397.n0127).
- Murton, B. J., B. Lehrmann, A. M. Dutrieux, S. Martins, A. G. de la Iglesia, I. J. Stobbs, F. J. Barriga, J. Bialas, A. Dannowski, and M. E. Vardy, 2019, Geological fate of seafloor massive sulphides at the TAG hydrothermal field (Mid-Atlantic Ridge): *Ore Geology Reviews*, **107**, 903–925, doi: [10.1016/j.oregeorev.2019.03.005](https://doi.org/10.1016/j.oregeorev.2019.03.005).
- Nakayama, K., and A. Saito, 2016, The seabed TDEM towed by ROV for the ocean bottom hydrothermal deposits: Near Surface Geoscience 2016-First Conference on Geophysics for Mineral Exploration and Mining, doi: [10.3997/2214-4609.201602109](https://doi.org/10.3997/2214-4609.201602109).
- Nozaki, T., T. Nagase, Y. Takaya, T. Yamasaki, T. Otake, K. Yonezu, K. Ikehata, S. Totsuka, K. Kitada, Y. Sanada, Y. Yamada, J. Ishibashi, H. Kumagai, L. Maeda, and the D/V Chikyu Expedition 909 Scientists, 2021, Subseafloor sulphide deposit formed by pumice replacement mineralisation: *Scientific Reports*, **11**, 8809, doi: [10.1038/s41598-021-87050-z](https://doi.org/10.1038/s41598-021-87050-z).
- Nozaki, T., T. Nagase, T. Ushikubo, K. Shimizu, J. Ishibashi, and the D/V Chikyu Expedition 909 Scientists, 2020, Microbial sulfate reduction plays an important role at the initial stage of subseafloor sulfide mineralization: *Geology*, **49**, 222–227, doi: [10.1130/G47943.1](https://doi.org/10.1130/G47943.1).
- Petersen, S., P. M. Herzig, and M. D. Hannington, 2000, Third dimension of a presently forming VMS deposit: TAG hydrothermal mound, Mid-Atlantic Ridge, 26°N: *Mineralium Deposita*, **35**, 233–259, doi: [10.1007/s001260050018](https://doi.org/10.1007/s001260050018).
- Petersen, S., A. Krätschell, N. Augustin, J. Jamieson, J. R. Hein, and M. D. Hannington, 2016, News from the seabed — Geological characteristics and resource potential of deep-sea mineral resources: *Marine Policy*, **70**, 175–187, doi: [10.1016/j.marpol.2016.03.012](https://doi.org/10.1016/j.marpol.2016.03.012).
- Petersen, S., T. Monecke, A. Westhues, M. D. Hannington, J. B. Gemmill, R. Sharpe, M. Peters, H. Strauss, K. Lackschewitz, and N. Augustin, 2014, Drilling shallow-water massive sulfides at the Palinuro volcanic complex, Aeolian island arc, Italy: *Economic Geology*, **109**, 2129–2158, doi: [10.2113/econgeo.109.8.2129](https://doi.org/10.2113/econgeo.109.8.2129).
- Safipour, R., S. Hölz, M. Jegen, and A. Swidinsky, 2018, A first application of a marine inductive source electromagnetic configuration with remote electric dipole receivers: Palinuro Seamount, Tyrrhenian Sea: *Geophysical Prospecting*, **66**, 1415–1432, doi: [10.1111/1365-2478.12646](https://doi.org/10.1111/1365-2478.12646).
- Sibuet, J.-C., J. Letouzey, F. Barbier, J. Charvet, J.-P. Foucher, T. W. C. Hilde, M. Kimura, L.-Y. Chiao, B. Marsset, C. Muller, and J.-F. Stéphan, 1987, Back arc extension in the Okinawa Trough: *Journal of Geophysical Research: Solid Earth*, **92**, 14041–14063, doi: [10.1029/JB092iB13p14041](https://doi.org/10.1029/JB092iB13p14041).
- Spagnoli, G., M. Hannington, K. Bairlein, A. Hördt, M. Jegen, S. Petersen, and T. Laurila, 2016, Electrical properties of seafloor massive sulfides: *Geo-Marine Letters*, **36**, 235–245, doi: [10.1007/s00367-016-0439-5](https://doi.org/10.1007/s00367-016-0439-5).
- Swidinsky, A., S. Hölz, and M. Jegen, 2012, On mapping seafloor mineral deposits with central loop transient electromagnetics: *Geophysics*, **77**, no. 3, E171–E184, doi: [10.1190/geo2011-0242.1](https://doi.org/10.1190/geo2011-0242.1).
- Takai, K., M. J. Mottl, S. H. Nielsen, and E. 331 Scientists, 2011, Proceedings of the Integrated Ocean Drilling Program: Integrated Ocean Drilling Program Management International Inc.
- Tornos, F., J. M. Peter, R. Allen, and C. Conde, 2015, Controls on the siting and style of volcanogenic massive sulphide deposits: *Ore Geology Reviews*, **68**, 142–163, doi: [10.1016/j.oregeorev.2015.01.003](https://doi.org/10.1016/j.oregeorev.2015.01.003).
- Totsuka, S., K. Shimada, T. Nozaki, J.-I. Kimura, Q. Chang, and J. Ishibashi, 2019, Pb isotope compositions of galena in hydrothermal deposits obtained by drillings from active hydrothermal fields in the middle Okinawa Trough determined by LA-MC-ICP-MS: *Chemical Geology*, **514**, 90–104, doi: [10.1016/j.chemgeo.2019.03.024](https://doi.org/10.1016/j.chemgeo.2019.03.024).
- Von Herzen, R. P., J. Kirklin, and K. Becker, 1996, Geoelectrical measurements at the TAG hydrothermal mound: *Geophysical Research Letters*, **23**, 3451–3454, doi: [10.1029/96GL02077](https://doi.org/10.1029/96GL02077).
- Wheelock, B., S. Constable, and K. Key, 2015, The advantages of logarithmically scaled data for electromagnetic inversion: *Geophysical Journal International*, **201**, 1765–1780, doi: [10.1093/gji/ggv107](https://doi.org/10.1093/gji/ggv107).
- Zhdanov, M. S., 2010, Electromagnetic geophysics: Notes from the past and the road ahead: *Geophysics*, **75**, no. 5, 75A49–75A66, doi: [10.1190/1.3483901](https://doi.org/10.1190/1.3483901).
- Zierenberg, R. A., Y. Fouquet, D. J. Miller, J. M. Bahr, P. A. Baker, T. Bjerkgård, C. A. Brunner, R. C. Duckworth, R. Gable, and J. Gieskes, 1998, The deep structure of a sea-floor hydrothermal deposit: *Nature*, **392**, 485–488, doi: [10.1038/33126](https://doi.org/10.1038/33126).

Biographies and photographs of the authors are not available.